



PCCP

Structure of Ice Confined in Silica Nanopores

Journal:	<i>Physical Chemistry Chemical Physics</i>
Manuscript ID	CP-ART-02-2021-000686.R1
Article Type:	Paper
Date Submitted by the Author:	04-May-2021
Complete List of Authors:	Mohammed, Sohaib; Cornell University, Civil and Environmental Engineering Asgar, Hassnain; Cornell University, School of Civil and Environmental Engineering Benmore, Chris; Argonne National Laboratory, Gadikota, Greeshma; Cornell University,

SCHOLARONE™
Manuscripts

1
2
3
4
5
6
7
8
9
10
11
12
13
14
15
16
17
18
19
20
21
22
23
24

Structure of Ice Confined in Silica Nanopores

Sohaib Mohammed,¹ Hassnain Asgar,¹ Chris J. Benmore,² and Greeshma Gadikota^{1,}*

¹School of Civil and Environmental Engineering, Cornell University. Ithaca, New York
14853, United States

²Advanced Photon Source, Argonne National Laboratory, Lemont, Illinois 60439, United
States

Abstract

* Corresponding Author. Phone: +1 607-255-4796. E-mail: gg464@cornell.edu

1 Observed anomalous thermodynamic properties of confined water such as deviations in the
2 melting point and freezing point motivate the determination of the structure of confined water as
3 a function of pore size and temperature. In this study, we investigate the dynamic evolution of
4 the structure of confined ice in SBA-15 materials with pore diameters of 4 nm, 6 nm, and 8 nm at
5 temperatures ranging from 183 K to 300 K using *in-operando* Wide-Angle X-Ray Scattering
6 (WAXS) measurements, X-Ray Partial Distribution Function (PDF) measurements, and classical
7 Molecular Dynamics (MD) simulations. Formation of hexagonal ice structures is noted in all the
8 three pore sizes. In silica nanopores with diameters of 4 nm, cubic ice formation is noted in
9 addition to hexagonal ice. Longer lasting hydrogen bonds and longer residence times of the
10 water molecules in the first coordination shell contribute to observed crystalline organization of
11 ice in confinement. Self-diffusion coefficients of confined liquid water predicted from classical
12 Molecular Dynamics (MD) simulations are four orders of magnitude higher compared to ice
13 formed in confinement. These experimental and simulation results provide comprehensive
14 insights underlying the organization of confined water and ice in silica nanopores and the
15 underlying physico-chemical interactions that contribute to the observed structures.

16

17 **Keywords:** water; ice; silica; pores, confinement; molecular dynamics, Wide Angle X-Ray
18 Scattering (WAXS) measurements

19

20

21

22 **1. Introduction**

1 Advancing predictive insights into ice hydrate formation can resolve several
2 technological challenges associated with achieving sustained fluid flow in subsurface
3 environments,¹⁻³ stability of hydrates in a changing climate,⁴ and in harnessing gas hydrate
4 formation mechanisms to store or recover gases of interest.⁵ While there is an extensive
5 understanding of the thermodynamics and phase transitions associated with bulk water and ice,
6 there is a limited fundamental understanding of the structure and organization of nano-confined
7 water and ice that contributes to anomalous thermodynamic behavior of nano-confined water
8 including the lower equilibrium melting point⁶⁻⁸ and disordered hydrogen bonding networks of
9 nanoconfined water⁹⁻¹¹ compared to bulk water.

10 To probe the molecular scale basis of observed deviations in the phase transitions of
11 confined water, the development of innovative and robust hybrid experimental and molecular
12 simulation approaches is needed. Developing novel methods to understand the phase behavior of
13 confined fluids can pave the way to design fluids with specific thermophysical properties for
14 customized chemical, physical and biological applications. With this context, the liquid-solid
15 phase transitions of confined water have been studied using various experimental and theoretical
16 techniques such as vapor pressure measurements, dilatometry, differential scanning calorimetry
17 (DSC), nuclear magnetic resonance (NMR) spectroscopy, X-ray and neutron diffraction and
18 molecular simulations.¹²⁻²² Silica nanopores have been used as confining environments to
19 investigate the phase transitions of confined water, since these materials provide well-defined
20 arrays of monodisperse cylindrical nanopores with tunable diameters ranging from 1 nm to 10
21 nm.^{23, 24} Further, synthetic silica materials serve as an analog to siliceous matter that is abundant
22 in the natural and subsurface geologic environments.

1 Several advancements have been made towards our understanding of the thermodynamics
2 of confined water on freezing. The enhancement in the melting point depression of confined
3 water as the pore diameter decreases^{6, 13, 25, 26} and the coexistence of liquid-solid phases in the
4 pore space at temperatures below the melting point of confined water¹⁵ have been experimentally
5 established. The concept of premelted water at the surface walls and its influence on the melting
6 behavior of confined water was proposed.^{15, 27, 28} Modifications to predictive relationships such
7 as the Gibbs-Thompson (GT) equation were developed based on these insights. According to the
8 modified GT equation, the melting point $T_m(R)$ of confined water decreases as a function of the
9 confinement space volume, $T_m(R) = T_m^{bulk} - \frac{K_{GT}}{R-d}$, where T_m^{bulk} is 273.15 K, K_{GT} is 53 ± 1 K nm,
10 R is the confinement radius and d is the premelted water layer between the confined ice and pore
11 wall which is about 0.4-0.7 nm.⁷ Although the modified GT equation predicted the influence of
12 the extent of confinement on the melting point and suggested the liquid-solid coexistence, it does
13 not provide fundamental insights into several ambiguous aspects of the phase transition nature of
14 the confined water such as the effect of surface chemistry and the chemical potential on the
15 melting point profile.

16 In this context, the liquid-solid phase transition nature of confined water and the emerged
17 ice structures in carbon nanotubes with diameters ranging from sub-nanometers to about 2 nm
18 have shown profound deviations from bulk water such as the emergence of multiple ice
19 polymorphs and the depression/elevation in the melting/freezing temperatures.²⁹⁻³² For instance,
20 Takaiwa and co-workers³³ showed that confined water in nanotubes with diameters ranging from
21 0.9 nm to 1.7 nm form at least nine ice polymorphs at 0 K. Koga et al.³⁴ revealed that four ice
22 polymorphs are spontaneously emerged from liquid-like disordered phases confined in nanotubes
23 with a diameter of 1.4 nm at 200 K. Pugliese et al.³⁵ linked the freezing point of confined water

1 in carbon nanotubes to the nanotube diameter by investigating the state of water in nanotubes
2 with diameters ranging from 0.98 nm to 1.37 nm. The results indicated that freezing points of
3 confined water in nanotubes with diameter of 1.056 nm is 390 K. Agrawal and co-workers³⁶
4 reported that the freezing transition of confined water in carbon nanotubes with diameters of
5 1.05-1.52 nm decreases as the pore diameter increases with the highest transition temperature of
6 105-115 °C in the nanotube of 1.05 nm. Although these anomalies are well established in
7 synthetic carbon nanotubes, the phase transitions nature and ice structure of confined water in
8 earth-abundant porous silica materials are far less understood.

9 Despite previous experimental and computational studies are performed on the phase
10 transition of confined water in silica-based materials,^{25, 27, 37-39} uncertainties in the structure and
11 dynamics of confined water still exist. The phase transition of confined water in silica pores with
12 a wide range of pore diameters and geometries has been found to obey a first-order transition,⁷
13 while other studies suggest that the transition occurs continuously.⁴⁰ Although several studies
14 have linked the melting point depression of confined water to the pore sizes and shapes,⁴¹
15 insights into the effect of the confining environment on the emergence of different ice
16 polymorphs are still lacking.

17 To address these uncertainties, we investigate the structure and organization of water
18 confined in silica nanopores using *in-situ* synchrotron Wide Angle X-Ray Scattering (WAXS)
19 measurements, X-Ray Pair Distribution Function (PDF) measurements, and classical molecular
20 dynamics (MD) simulations. Experiments and simulations are performed on confined water in
21 cylindrical SBA-15 silica pores with diameters of 4 nm, 6 nm, and 8 nm, and at temperatures in
22 the range of 183 K - 300 K to probe insights on the structure and dynamics of supercooled water
23 in confinement and the associated phase transitions in this temperature range. The hypothesis

1 that the differences in the hydrogen bonding of confined water molecules influence the structure
2 of confined water is probed. Thus, this study aims to provide insights derived from experiments
3 and simulations into the structure of ice as a function of confinement and temperature and the
4 underlying hydrogen bonding behavior that contributes to the observed organization of confined
5 water.

6 **2. Methods**

7 **2.1. Experimental determination of the structural features of ice**

8 The structures of ice formed in silica nanopores are determined using *in-situ* Wide Angle
9 X-Ray Scattering (WAXS) measurements. Water is loaded in the powdered SBA-15 materials
10 with pore diameters of 4 nm, 6 nm, and 8 nm (Sigma Aldrich). These SBA-15 materials
11 comprise interconnected cylindrical pores with parallel alignment (**see Figure 1 (a)**). The silica
12 materials are dried at 130 °C for 2 hours to remove the adsorbed water and impurities and then
13 loaded with water. This drying protocol aimed to remove the physically adsorbed water on the
14 SBA-15 surface rather than the chemically bound OH groups on the pores' surfaces. The SBA-
15 15 materials loaded with water are filled in quartz capillaries with outer and inner diameters of
16 1.5 mm and 1.2 mm, respectively. The capillaries are loaded in the instrument and the samples
17 are supercooled using liquid N₂ to 183 K using a cryostream cooler (Oxford cryo-stream 700).
18 The samples are subsequently heated to room temperature (300 K) and measurements are taken
19 during heating. To capture temperature-dependent changes in the confined water structure, the
20 data are collected at 183 K, 200 K, 220 K, 240 K, 255 K, 273 K and 300 K. The samples are
21 equilibrated for 10 minutes at each temperature before data acquisition. After the data
22 acquisition, the samples are heated to the subsequent temperature.

1 WAXS measurements are performed at Beamline 6-ID-D in Sector 6 at Advanced Photon
2 Source (APS) at Argonne National Laboratory (ANL).⁴² The incident X-ray beam used has a
3 wavelength of 0.206592 Å and an energy of 60 keV. During the measurements, the Varex
4 CT4343 detectors are utilized to collect the scattered beam from the samples and the sample-to-
5 detector distance for the WAXS measurements is 385.4 mm. The instrument calibrations are
6 performed on a cerium dioxide (CeO₂) reference sample.^{43, 44} The WAXS data are reduced using
7 NIKA⁴⁵ algorithm embedded in Igor software (WaveMetrics) and the scattered intensity at each
8 temperature is plotted as a function of the wavevector (Q) (where $Q = (4\pi/\lambda) \sin \theta$, λ is the X-ray
9 wavelength, and θ is half of the scattering angle). Background from the empty capillary at each
10 temperature is also acquired and subtracted from the scattering intensities obtained from the
11 samples in the capillary.

12 X-ray differential pair distribution functions ($D(r)$) are extracted and fitted from Small-
13 Angle and Wide-Angle X-Ray Scattering (SAXS/WAXS) measurement using fit2D software.⁴⁶
14 The data are reduced, combined, and normalized to the form factor calculations of Wang and co-
15 workers⁴⁷ as noted by Skinner and co-workers.⁴⁴ X-ray differential pair distribution function is
16 calculated as follows, where ρ , r and $g(r)$ are the density, radius, and the measured pair
17 distribution function, respectively:

$$18 \quad D(r) = 4\pi\rho r [g(r) - 1] \quad (1)$$

19 The obtained $D(r)$ contains the O-O and O-H interactions in the confined water molecules in 4
20 nm, 6 nm and 8 nm sized pores.

21 **2.2. Molecular dynamics (MD) simulations of the structure of ice**

1 The molecular scale mechanisms underlying the observed structure of ice are determined
2 using classical MD simulations. To obtain representative pore structures, cylindrical pores
3 terminated by -OH groups with diameters of 4 nm, 6 nm, and 8 nm are cleaved in silica surfaces
4 to obtain the material architectures representative of the X-ray scattering measurements (**Figure**
5 **1 (b)**). The -OH group density on the pore surface is about 8 nm^{-2} .^{48, 49} The 4 nm, 6 nm and 8 nm
6 pores were filled with 592, 1571 and 2962 water molecules, respectively, to achieve a water
7 density of about 1 g/cm^3 . The silica pores and water molecules are modeled using ClayFF⁵⁰ and
8 TIP5P⁵¹ models (**see Table S1**) and the potentials account for the bonded and nonbonded
9 interactions. ClayFF accounts for the nonbonded interactions between the silica atoms and the
10 $\text{O}_{\text{nonbridging}}\text{-H}$ bonds stretching only. TIP5P model is a five-site potential composed of Lennard
11 Jones (LJ) sites on the neutral oxygen, two positively charged hydrogens and two negatively
12 charged massless sites. The melting point of TIP5P model is 274 K at 1 bar which is consistent
13 with the experimental melting point of bulk water (273.15 K).⁵² The TIP5P model has been used
14 extensively to model the behavior of water at low temperatures.⁵³⁻⁵⁵

15 The constructed initial configurations were optimized for geometry using the steepest
16 descent method for 50,000 steps. Simulated annealing algorithms are performed on the optimized
17 configurations under a constant number of particles, constant volume, and constant temperature
18 (NVT) ensemble for 120 ns. The system is equilibrated at 300 K, steeply quenched to 183 K
19 followed a systematic steep heating to 200 K, 220 K, 230 K, 235 K, 240 K, 245 K, 250 K, 255
20 K, 273 K and 300 K with 10 ns equilibrium time at each temperature point to be consistent with
21 the experimental WAXS measurements (**see Figure S1**). The leapfrog integrator with a time step
22 of 1 fs is utilized to solve the equation of motion. Nose-Hoover thermostat is used to control the
23 simulation temperature.^{56, 57} The short-range interactions are calculated within a cutoff of 1.2 nm,

1 while the long-range electrostatic interactions are treated using Particle Mesh Ewald (PME).⁵⁸
 2 During the MD simulation, bonding interactions accounted for bond stretching, angles bending
 3 and dihedrals, while nonbonding interactions are calculated for van der Waals (vdW) and
 4 electrostatic (ES) interactions. vdW and ES interactions are modeled using 12-6 LJ and

5 Coulomb's functions, respectively, as follows: $U_{ij} = \sum_{i < j} \left[4\varepsilon_{ij} \left[\left(\frac{\sigma_{ij}}{r_{ij}} \right)^{12} - \left(\frac{\sigma_{ij}}{r_{ij}} \right)^6 \right] + \frac{q_i q_j}{4\pi\varepsilon_o r_{ij}} \right]$ where

6 ε_{ij} is the potential well depth, σ_{ij} is the finite distance at which the interatomic distance is zero,
 7 r_{ij} is the distance between i and j , q_i and q_j are the charges of i and j , and ε_o is the dielectric
 8 permittivity of vacuum. LJ parameters (i.e., ε_{ij} and σ_{ij}) for unlike molecular interactions are

9 calculated based on the Lorentz-Berthelot rule as follows: $\sigma_{ij} = \frac{\sigma_{ii} + \sigma_{jj}}{2}$ and $\varepsilon_{ij} = \sqrt{\varepsilon_{ii}\varepsilon_{jj}}$. MD

10 simulations are performed using GROMACS 2018 software.⁵⁹

11 **3. Results and Discussions**

12 **3.1. The temperature-dependent structure of confined water**

13 The hypothesis that the structure of ice in confinement varies with pore diameter is
 14 probed experimentally using *in-situ* WAXS measurements. The *in-situ* WAXS intensity curves
 15 of water confined in 4 nm, 6 nm and 8 nm sized silica pores as a function of the Q at
 16 temperatures ranging from 183 K to 300 K are shown in **Figure 2**. The main peaks in the
 17 intensity curves, at Q in the range of of 2 \AA^{-1} to 3 \AA^{-1} for 4 nm, 6 nm and 8 nm pores,
 18 respectively, are fitted using Lorentzian function to probe the full width half maximum (fwhm)
 19 to quantitatively analyze the changes in the intensity of the peaks as a function of temperature
 20 (see **Figure S2**).

1 The WAXS profiles demonstrate a clear dependence of the structure of ice on pore
2 diameters of 4 nm, 6 nm, and 8 nm and temperatures ranging from 183 K to 255 K. Significant
3 shifts in the peak positions are not detected, though new peaks arise as the temperatures change
4 from 183 K to 273 K. These data show that stable ice structures are formed at temperatures
5 below the melting point of the confined ice, which is consistent with the findings of Morishige
6 and co-workers.⁶⁰ Ice structures are a function of the pore size. Cubic ice and hexagonal ice are
7 formed in silica nanopores with pore diameters of 4 nm. The formation of mixture of hexagonal
8 and cubic ice in 4 nm pores is consistent with the findings of Thangswamy and co-workers⁶¹ who
9 studied the evolution of ice structure in 2.5 nm cylindrical silica pores. Thangswamy et al.
10 attributed the formation of mixture of hexagonal and cubic ice to the nucleation of ice crystals
11 inside the pore at low temperatures (below 240 K) that creep out of the pores to form bulk
12 crystals with hexagonal and cubic polymorphs. In contrast, hexagonal ice is formed in pores with
13 diameters of 6 nm and 8 nm. These observed structures of ice in confinement are consistent with
14 previous studies.^{62, 63} The intensity of the peaks representing crystalline ice is significantly
15 reduced after 255 K and these peaks disappear at 300 K in all the pore sizes, suggesting the total
16 melting of the formed ice.

17 The temperature-dependent structural alterations of the confined water are also evident
18 from the profiles of the experimentally obtained X-Ray Differential Pair Distribution Functions
19 (PDF) represented by $D(r)$ (see **Figure 3**) and radial distribution functions determined from
20 molecular dynamics (MD) simulations represented by $g(r)$ (see **Figure 4 (a-c)**). Water confined
21 in 4 nm sized pore formed single crystals of ice, thus a reliable differential pair distribution
22 functions could not be extracted. The temperature-dependent $D(r)$ profiles show well defined
23 peaks for the first and second shells at about 2.8 Å and 4.6 Å, respectively. As the temperature

1 increases, the first peak shifts to longer distances and the second shell decreases in intensity as
2 the confined water adopts a more tetrahedral structure.⁶⁴ At 300 K, $D(r)$ shows similar local
3 structural arrangements of confined water in all the pores with broadening of the first peak
4 between 8 nm and 6 nm (see **Figure S3**).

5 The respective positions of the first and second coordination shells corresponding to the
6 organization of water are calculated to be $2.78 \pm 0.03 \text{ \AA}$ and $4.52 \pm 0.02 \text{ \AA}$, respectively, in 4 nm,
7 6 nm and 8 nm sized pores (see **Figure 4 (a-c)**). These positions are obtained from the radial
8 distribution profiles, $g(r)$ using molecular dynamics simulations (see **Figure 4 (a-c)**). The
9 systematic arrangement of water molecules with decreasing temperature is evident from the
10 increasing intensity of the peak that corresponds to the first coordination shell. The rate of
11 increase in the peak that corresponds to the first coordination shell is $0.000259 \pm 0.000014 \text{ \AA K}^{-1}$,
12 $0.000482 \pm 0.000021 \text{ \AA K}^{-1}$ and $0.000314 \pm 0.000018 \text{ \AA K}^{-1}$ in 4 nm, 6 nm, and 8 nm sized
13 pores, respectively. The peak positions that correspond to the first and second coordination shells
14 and the rates of change with temperature agree with prior experimental and simulation results
15 after accounting for confinement effects.⁶⁴⁻⁶⁸ These studies are summarized in **Table 1**.

16 The transition of ordered polymorphs of ice at low temperatures to amorphous structures
17 and a decrease in the number of molecules in the first hydration shell of water with increasing
18 temperature is evident from the reduction of $g(r)$ peak height (**Figure 4**). Changes in the
19 structure and density of interfacial water are evident from the $g(r)$ representing the O-O
20 coordination of water at the silica surface (see **Figure S4**).

21 The oxygen-oxygen coordination number ($n_{oo}(r)$) (**Figure 4 (d-f)**) was also calculated to
22 determine the number of atoms with the distance r by integrating $g(r)$ as follows:

$$n_{oo}(r) = 4\pi\rho \int_0^r r^2 g(r) dr \quad (2)$$

In the expression above, ρ is the number density of confined water (determined as the total number of molecules divided by the pore volume). The profiles of n_{oo} indicates the existence of isosbestic point in the applied range of temperatures. Isosbestic point is defined as the point at which the probability of finding an oxygen atom surrounding another oxygen atom is constant with temperature.^{66, 67} The position of the isosbestic point for confined water is comparable to that of bulk water, which is consistent with previous studies.^{64, 67} However, the corresponding n_{oo} of confined water is lower than that of bulk water over the same range of temperatures. The oxygen-oxygen coordination number, $n_{oo}(r)$ is 4.39 ± 0.15 and 4.3 ± 0.3 at the range 234-366 K as suggested by Pathak and co-workers⁶⁷ and Skinner and co-workers,⁶⁶ respectively. The observation of the isosbestic point implies that the first coordination shell of confined water shifts slightly from 2.72 Å (the position of the first peak) to 3.25 Å (the position of the isosbestic point) as the temperature changes from 183 K to 300 K. In other words, the number of molecules in the first shell remains constant within the isosbestic point radius and does not exchange with the outer shells which consequently implies that the hydrogen bonding rearrangement occurs separately within each shell defined as below or above 3.25 Å.⁶⁷ Further, the transition in the structure of confined water at 255 K is also evident from the coordination number profiles as the flattening in the n_{oo} curves in the radius between 2.8 Å and 3.4 Å decreases substantially and the curves become more linear with the radius after 255 K (see **Figure 4 (d-f)**).

The tetrahedral structure of ice and the absence of interstitial water molecule and additional neighbor molecules in the first coordination shell of water molecules⁶⁹ is evident from the plateau around a coordination number of 3.7 at low temperatures of 183-255 K. The

1 existence of interstitial water molecules at 273 K and 300 K is evident from the absence of this
2 plateau, which is consistent with structure of amorphous water.^{43, 70} The formation of structured
3 ice at low temperatures is also observed from the MD simulations (see **Figure 5** and **Figure 6**).
4 **Figure 5** shows snapshots of the front and side views of the hexagonal and cubic structures of
5 ice that extend along the pore length (z-direction). At low temperatures of 183 K and 200 K, the
6 hexagonal ice structures are abundant in the 4 nm, 6 nm and 8 nm pores.

7 The fraction of hexagonal ice formed in confinement decreases slightly as the
8 temperature increases to 255 K and totally disappears at 300 K, as indicated by the 2D density
9 maps of the confined water molecules in 4 nm, 6 nm and 8 nm pores that obtained from MD
10 simulations (see **Figure 6**). The low-density and high-density regions that stem from the
11 formation of structured water are evident at 200 K in all the pores. The contrast between the low-
12 density and high-density regions start to decrease at 250 K due to the breaking of the formed
13 structures at lower temperatures and the emergence of amorphous structures. On heating the
14 systems to 300 K, all the formed structures at 200 K disappear and the only observed contrast in
15 the pore is between the interfacial water and free confined water. At 300 K, the interfacial water
16 showed higher densities due to the favorable interaction with the hydrophilic silica surface which
17 is consistent with previous MD simulation studies.⁷¹⁻⁷³ It is interesting to observe that the
18 contrast between the interfacial water and free water decrease significantly at low temperatures,
19 suggesting that the surface effect on the confined water increases with temperature.

20 **3.2. The nature of the phase transition of confined water**

21 In addition to the structural characteristics of the confined water, the hydrogen bonding
22 nature between the water molecules, both the free water and the interfacial water at the pore
23 surface, provide critical insights into the nature of the phase transition and the local structure of

1 the water molecules in the temperature range of interest which is 183 K – 300 K. Our
2 calculations from molecular dynamics simulations showed that the the number of hydrogen
3 bonds per confined water molecule increases steeply from slightly less than 2 to about 3.3 as the
4 temperature decreased from 300 K to 183 K (**see Figure 7 (a)**). The steep change in the
5 hydrogen bonds as the system is quenched suggests a first-order transition of confined water in 4
6 nm, 6 nm, and 8 nm pore sizes which is consistent with previous studies.^{11, 55, 74} The number of
7 hydrogen bonds per water molecule at temperatures between 183 K and 230 K is greater than 3,
8 indicating the formation of 3D water networks in confinement. The number of hydrogen bonds
9 per confined water molecule decreases continuously from about 3.3 to about 2.7 as the
10 temperature increases from 183 K to 255 K. First-order transitions are also noted on heating the
11 confined water from 255 K to 273 K and from 273 K to 300 K where the number of hydrogen
12 bonds decreased to about 2.3 and to about 1.9, respectively. These two first-order transitions are
13 also evident from the WAXS intensities and the $D(r)$ profiles with an increase in the temperature
14 (**see Figure 2 and Figure 3**).

15 The formed hydrogen bonds between free water molecules exhibit a lifetime of about 2
16 ns at low temperatures of 183 K (**see Figure S5**). The average lifetime of the water-water
17 hydrogen bonds decreased slightly as the system was heated to about 240 K, followed by a
18 dramatic decrease to reach about 0.003 ns at 273 K and 300 K. The long-lasting hydrogen bonds
19 at low temperatures indicate the formation of stable clusters in the confined water outside the
20 interfacial water layer.

21 Interfacial hydrogen bonding with the hydroxyl groups on the pore surface reduce the
22 number of hydrogen bonds formed between the free water molecules. The number of hydrogen
23 bonds between the interfacial water layer and the OH groups on the pore surface increases with

1 the pore diameter due to the increase in the number of the OH groups on the surface (see **Figure**
2 **7 (b)**). Interestingly, the phase transitions of confined free water molecules differ from that of
3 water molecules bonded to the pore surfaces. The hydrogen bonding of interfacial water showed
4 temperature-independent profiles in 4 nm, 6 nm and 8 nm sized pores. The observed first-order
5 phase transitions of confined free water are not evident from the hydrogen bonding profiles of
6 interfacial water. The water-pore hydrogen bonds profiles indicate that the interfacial water layer
7 retain premelted water properties even at temperatures as low as 183 K which agrees with
8 previous studies.^{7, 8}

9 The stability of the formed water structures as the temperature changes and time taken
10 by water molecules to remain in contact with each other at each temperature are probed by
11 calculating the residence autocorrelation function ($C_R(t)$) (see **Figure 8**). The contact period of
12 the water molecules was monitored by computing $C_R(t)$ as follows^{75, 76}:

$$13 \quad C_R(t) = \frac{\langle O_w(t)O_w(0) \rangle}{\langle O_w(0)O_w(0) \rangle} \quad (3)$$

14 In the expression above, $O_w(t)$ describes whether the molecule is in the first coordination shell
15 of the water molecule at a time t , $O_w(t)$ is equal to one if the molecule exists in the first
16 coordination shell at time t , otherwise it equal to zero. The residence autocorrelation function is
17 calculated from the center of the mass of the water molecules. Faster decay of $C_R(t)$ from 1 to 0
18 is an indicative of the shorter contact between the water molecules. Longer decay time is evident
19 at low temperatures and the decay time systematically decreases with an increase in temperature.
20 A decay time of about 3.6 ns was noted at temperatures up to 240 K. A substantial decrease in
21 the decay time to less than 0.1 ns was noted at 300 K. The longer decay time at low temperatures
22 suggests that the water molecules in the first coordination shell exchange more slowly with those

1 from outside the first shell. The longer contact time of the water molecules facilitates the
2 rearrangement of the water molecules within the first coordination shell to form hydrogen
3 bonding networks that result in ice with crystalline structures. The trend in the contacting time
4 between the water molecules represented by $C_R(t)$ is consistent with the lifetime of hydrogen
5 bonds between the confined water molecules.

6 Similarities in the transitions associated with water-water hydrogen bonding profiles and
7 the potential energy of the confined water molecules are noted (see **Figures 7 (a) and 9 (a)**).
8 Potential energy represents the summation of bonded and nonbonded interactions of water
9 molecules, including bond stretchings, angle bendings, dihedrals, van der Waals and
10 electrostatic interactions. The potential energy of the confined free water molecules decreased
11 steeply by about 8 kJ/mol on quenching the systems from 300 K to 183 K which confirms the
12 first-order transition noted from the hydrogen bonding profiles (**Figure 7 (a)**). This drop in
13 potential energy is in agreement with the data corresponding to the freezing transition of bulk
14 water of 7 kJ/mol⁷⁷ and differs from that of confined water (5.6 kJ/mol)¹¹ predicted using TIP4P
15 models. This first-order phase transition is followed by a continuous increase in the potential
16 energy on heating the system from 183 K to 255 K, followed by two steep increases on heating
17 from 255 K to 273 K and from 273 K to 300 K, which implies two other first-order phase
18 transitions. The increase in the potential energy on heating the system from 255 K to 273 K and
19 from 273 K to 300 K is about 3 kJ/mol, which is comparable to that of the transition of confined
20 TIP5P nanofilms⁵⁵ and to the melting of bilayer ice.⁷⁸

21 Potential energy of the interfacial water molecules on the pore surface are dependent on
22 the size of the pore. Larger pores have more number of water molecules bound to the pore
23 surface which contribute to higher potential energy (the absolute value of the potential energy)

1 (see **Figure 9 (b)**). The negative sign of the potential energy indicates the attractive nature of
2 water-pore interactions. The potential energy profiles of interfacial water molecules (**Figure 9**
3 **(b)**) are less sensitive to changes in temperature compared the confined water molecules (**Figure**
4 **9 (a)**). The hydrogen bonding and potential energy profiles show that the first-order phase
5 transitions of the interfacial water molecules differ from that of confined water.

6

7 **3.3. The temperature-dependent dynamics of confined water**

8 To probe the changes in the dynamics of water confined in silica nanopores during
9 freezing, the diffusivities of confined water as a function of temperature are probed (see **Figure**
10 **10**). Prior studies demonstrated significant differences in the diffusivities of ice formed in
11 unconfined environments and in bulk water. For example, the diffusion coefficient of bulk ice is
12 $\sim 10^{-9}$ cm²/sec, while that of bulk liquid water is $\sim 10^{-5}$ cm²/sec.^{74, 79-81} However, few studies
13 have linked the phase transitions of confined water and structures of ice to the corresponding
14 diffusive transport behavior. The diffusivities of the confined water and ice differ by nearly four
15 orders of magnitude.

16 This orders of magnitude change in the diffusion coefficient at temperatures in the range of 183
17 K to 300 K is comparable to that of the liquid to crystalline ice transition obtained both
18 experimentally and computationally.^{11, 82} The diffusivity changes by less than one order of
19 magnitude between 183 K and 220 K followed by an increase of three orders of magnitude on
20 heating to 255 K. At 273 K and 300 K, the diffusivity plateaus at about 10^{-5} cm²/sec which is
21 consistent with that of bulk water.

22 The self-diffusion coefficients of confined water are dependent on the pore size with
23 larger pore sizes of 8 nm sizes having higher diffusivities compared to 6 nm and 4 nm pores.

1 These observations are consistent with observations that narrower pores contribute to lower
2 diffusivities of confined water at various surface chemistries.^{71, 83-85} Further, the mean square
3 displacement (MSD) profiles (see **Figure S6**) indicate a transition from a ballistic motion (
4 $MSD \propto t^2$), where t is the time, to a diffusive motion ($MSD \propto t$) at high temperatures, which is
5 a characteristic of typical liquid behavior.⁵⁵ At temperatures below the melting points, the MSD
6 profiles are less dependent on the time with time independent diffusivities noted at 183 K and
7 200 K in all the pore sizes, suggesting that all the confined water had turned to ice. The change
8 in the MSD profiles of confined water in 4 nm, 6 nm and 8 nm pores confirm the melting of the
9 formed ice inside the silica pores at higher temperatures which is in agreement with the
10 experimental diffraction measurements observed inside cylindrical silica nanopores.⁶³

11 **4. Conclusions**

12 Several important insights into the structure, organization, and nano-scale diffusivity of
13 confined water and ice in cylindrical silica pores with sizes of 4 nm, 6 nm, and 8 nm at
14 temperatures ranging from 183 K to 300 K are obtained using *in-situ* Wide-Angle X-Ray
15 Scattering (WAXS) measurements, X-Ray Pair Distribution Function (PDF) measurements and
16 classical molecular dynamics (MD) simulations. Hexagonal ice structures are dominant in silica
17 nanopores with diameters of 4 nm, 6 nm, and 8 nm. Cubic ice is noted in addition to hexagonal
18 ice in silica nanopores with a diameter of 4 nm. The formation of hexagonal crystalline ice is
19 confirmed using MD simulations. The profiles of hydrogen bonding and the potential energy
20 obtained from the MD simulations indicate the existence of multiphase transitions as the system
21 is quenched from 300 K to 183 K, heated from 255 K to 273 K, and from 273 K to 300 K. The
22 structure of the formed ice is characterized by longer lasting hydrogen bonds, the presence of
23 isosbestic point and longer contacting time with the molecules in the first coordination shell

1 compared to liquid water. These insights inform emerging efforts to tune the structure and
2 organization of hydrates for energy and environmental applications. The applied experimental-
3 computational method in this study can be extended to probe the properties of confined fluids in
4 a wide range of porous materials and to achieve a predictive controlling over the properties of
5 these fluids.

6 **Associated Content**

7 The supporting information file contains detailed description on the methods and supplementary
8 data supporting the finding of the paper including Wide Angle X-Ray Scattering (WAXS), X-
9 Ray Pair Distribution Function (PDF), hydrogen bonding lifetime, radial distribution functions
10 (RDFs), and the mean square displacement of water.

11 **Acknowledgment**

12 This work was supported as part of the Multi-Scale Fluid-Solid Interactions in Architected and
13 Natural Materials (MUSE), an Energy Frontier Research Center funded by the U.S. Department
14 of Energy, Office of Science, Basic Energy Sciences under Award # DE-SC0019285.

15 **References**

- 16 1. S. Dai, Y. Seol, *Geophys. Res. Lett.*, 2014, **41**, 4176-4184.
- 17 2. D. Wang, C. Wang, C. Li, C. Liu, H. Lu, N. Wu, G. Hu, L. Liu, Q. Meng, *Fuel*, 2018,
18 **226**, 516-526.
- 19 3. G. Li, L. Zhan, T. Yun, S. Dai, *Geophys. Res. Lett.*, 2020, **47**, e2020GL086990.
- 20 4. A. Portnov, S. Vadakkepuliambatta, J. Mienert, A. Hubbard, *Nat. Commun.*, 2016, **7**, 1-
21 7.

- 1 5. Z. R. Chong, S.H.B. Yang, P. Babu, P. Linga, X.S. Li, *Appl. Energ.*, 2016, **162**, 1633-
2 1652.
- 3 6. G. H. Findenegg, S. Jähnert, D. Akcakayiran, A. Schreiber, *ChemPhysChem*, 2008, **9**,
4 2651-2659.
- 5 7. S. Jähnert, F.V. Chávez, G.E. Schaumann, A. Schreiber, M. Schönhoff, G.H. Findenegg,
6 *Phys. Chem. Chem. Phys.*, 2008, **10**, 6039-6051.
- 7 8. E. B. Moore, E. De La Llave, K. Welke, D.A. Scherlis, V. Molinero, *Phys. Chem. Chem.*
8 *Phys.*, 2010, **12**, 4124-4134.
- 9 9. M. Matsumoto, S. Saito, I. Ohmine, *Nature*, 2002, **416**.
- 10 10. I. M. Svishchev, P.G. Kusalik, *J. Am. Chem. Soc.*, 1996, **118**, 649-654.
- 11 11. K. Koga, H. Tanaka, X.C. Zeng, *Nature*, 2000, **408**, 564.
- 12 12. O. Petrov, I. Furó, *Phys. Rev. E*, 2006, **73**, 011608.
- 13 13. A. Schreiber, I. Ketelsen, G.H. Findenegg, *Phys. Chem. Chem. Phys.*, 2001, **3**, 1185-
14 1195.
- 15 14. J. Jelassi, T. Grosz, I. Bako, M.C. Bellissent-Funel, J.C. Dore, H.L. Castricum, R. Sridi-
16 Dorbez, *J. Chem. Phys.*, 2011, **134**, 064509.
- 17 15. E. B. Moore, J.T. Allen, V. Molinero, *J. Phys. Chem. C*, 2012, **116**, 7507-7514.
- 18 16. F. G. Alabarse, J. Haines, O. Cambon, C. Levelut, D. Bourgogne, A. Haidoux, D.
19 Granier, B. Coasne, *Phys. Rev. Lett.*, 2012, **109**, 035701.
- 20 17. J. C. Van Miltenburg, J.P. Van der Eerden, *J. Cryst. Growth*, 1993, **128**, 1143-1149.
- 21 18. T. Takamuku, M. Yamagami, H. Wakita, Y. Masuda, T. Yamaguchi, *J. Phys. Chem. B*,
22 1997, **101**, 5730-5739.

- 1 19. D. Liu, Y. Zhang, C.C. Chen, C.Y. Mou, P.H. Poole, S.H. Chen, *P. Natl. Acad. Sci. USA*,
2 2007, **104**, 9570-9574.
- 3 20. Z. Wang, K. Ito, J.B. Leão, L. Harriger, Y. Liu, S.H. Chen, *J. Phys. Chem. Lett.*, 2015, **6**,
4 2009-2014.
- 5 21. B. R. Puri, D.D. Singh, Y.P. Myer, *T. Faraday Soc.*, 1957, **53**, 530-534.
- 6 22. A. A. Antoniou, *J. Phys. Chem. B*, 1964, **68**, 2754-2763.
- 7 23. Z. Wang, K.H. Liu, L. Harriger, J.B. Leão, S.H. Chen, *J. Chem. Phys.*, 2014, **141**,
8 014501.
- 9 24. F. Mallamace, C. Corsaro, D. Mallamace, Z. Wang, S.H. Chen, *Front. Phys.*, 2015, **10**,
10 p.106103.
- 11 25. K. Morishige, H. Iwasaki, *Langmuir*, 2003, **19**, 2808-2811.
- 12 26. E. Tombari, G. Salvetti, C. Ferrari, G.P. Johari, *J. Chem. Phys.*, 2005, **122**, p.104712.
- 13 27. E. W. Hansen, M. Stöcker, R. Schmidt, *J. Phys. Chem.*, 1996, **100**, 2195-2200.
- 14 28. A. Endo, T. Yamamoto, Y. Inagi, K. Iwakabe, T. Ohmori, *J. Phys. Chem. C*, 2008, **112**,
15 9034-9039.
- 16 29. M. Raju, A. Van Duin, M. Ihme, *Sci. Rep.*, 2018, **8**, 1-11.
- 17 30. J. Shiomi, T. Kimura, S. Maruyama, *J. Phys. Chem. C*, 2007, **111**, 12188-12193.
- 18 31. T. Ohba, *J. Phys. Chem. C*, 2020, **124**, 14213-14219.
- 19 32. Y. Maniwa, H. Kataura, M. Abe, A. Udaka, S. Suzuki, Y. Achiba, H. Kira, K. Matsuda,
20 H. Kadowaki, Y. Okabe, *Chem. Phys. Lett.*, 2005, **401**, 534-538.
- 21 33. D. Takaiwa, I. Hatano, K. Koga, H. Tanaka, *P. Natl. Acad. Sci. USA*, 2008, **105**, 39-43.
- 22 34. K. Koga, G.T. Gao, H. Tanaka, X.C. Zeng, *Physica A*, 2002, **314**, 462-469.

- 1 35. P. Pugliese, M.M. Conde, M. Rovere, P. Gallo, *J. Phys. Chem. B*, 2017, **121**, 10371-
2 10381.
- 3 36. K. V. Agrawal, S. Shimizu, L.W. Drahushuk, D. Kilcoyne, M.S. Strano, *Nat.*
4 *Nanotechnol.*, 2017, **12**, 267.
- 5 37. J. Deschamps, F. Audonnet, N. Brodie-Linder, M. Schoeffel, C. Alba-Simionesco, *Phys.*
6 *Chem. Chem. Phys.*, 2010, **12**, 1440-1443.
- 7 38. X. X. Liu, Q. Wang, X.F. Huang, S.H. Yang, C.X. Li, X.J. Niu, Q.F. Shi, G. Sun, K.Q.
8 Lu, *J. Phys. Chem. B*, 2010, **114**, 4145-4150.
- 9 39. K. Morishige, K. Nobuoka, *J. Chem. Phys.*, 1997, **107**, 6965-6969.
- 10 40. M. Erko, G.H. Findenegg, N. Cade, A.G. Michette, O. Paris, *Phys. Rev. B*, 2011, **84**,
11 104205.
- 12 41. Y. Xia, H. Cho, M. Deo, S.H. Risbud, M.H. Bartl, S. Sen, *Sci. Rep.*, 2020, **10**, 1-8.
- 13 42. C. J. Benmore, O.L.G. Alderman, D. Robinson, G. Jennings, A. Tamalonis, J. Ilavsky, E.
14 Clark, E. Soignard, J.L. Yarger, J.K.R. Weber, *Nucl. Instrum. Meth. A*, 2020, **955**,
15 163318.
- 16 43. D. Mariedahl, F. Perakis, A. Späh, H. Pathak, K.H. Kim, G. Camisasca, D. Schlesinger,
17 C. Benmore, L.G.M. Pettersson, A. Nilsson, K. Amann-Winkel, *J. Phys. Chem. B*, 2018,
18 **122**, 7616-7624.
- 19 44. L. B. Skinner, C. Huang, D. Schlesinger, L.G. Pettersson, A. Nilsson, C.J. Benmore, *J.*
20 *Chem. Phys.*, 2013, **138**, 074506.
- 21 45. J. Ilavsky, *J. Appl. Crystallogr.*, 2012, **45**, 324-328.
- 22 46. A. P. Hammersley, S.O. Svensson, M. Hanfland, A.N. Fitch, D. Hausermann, *Int. J. High*
23 *Press. Res.*, 1996, **14**, 235-248.

- 1 47. J. Wang, A.N. Tripathi, V.H. Smith Jr, *J. Chem. Phys.*, 1994, **101**, 4842-4854.
- 2 48. L. T. Zhuravlev, *Langmuir*, 1987, **3**, 316-318.
- 3 49. B. Siboulet, B. Coasne, J.F. Dufrêche, P. Turq, *J. Phys. Chem. B*, 2011, **115**, 7881-7886.
- 4 50. R. T. Cygan, J.J. Liang, A.G. Kalinichev, *J. Phys. Chem. B*, 2004, **108**, 1255-1266.
- 5 51. M. W. Mahoney, W.L. Jorgensen, *J. Chem. Phys.*, 2000, **112**, 8910-8922.
- 6 52. C. Vega, E. Sanz, J.L.F. Abascal, *J. Chem. Phys.*, 2005, **122**, 114507.
- 7 53. D. T. Limmer, D. Chandler, *Faraday Discuss.*, 2013, **167**, 485-498.
- 8 54. P. Kumar, F.W. Starr, S.V. Buldyrev, H.E. Stanley, *Phys. Rev. E*, 2007, **75**, 011202.
- 9 55. S. Han, M.Y. Choi, P. Kumar, H.E. Stanley, *Nat. Phys.*, 2010, **6**, 685-689.
- 10 56. S. Nosé, *Mol. Phys.*, 1984, **52**, 255-268.
- 11 57. W. G. Hoover, *Phys. Rev. A*, 1985, **31**, 1695.
- 12 58. T. Darden, D. York, L. Pedersen, *J. Chem. Phys.*, 1993, **98**, 10089-10092.
- 13 59. M. J. Abraham, T. Murtola, R. Schulz, S. Páll, J.C. Smith, B. Hess, E. Lindahl,
14 *SoftwareX*, 2015, **1**, 19-25.
- 15 60. K. Morishige, H. Yasunaga, H. Uematsu, *J. Phys. Chem. C*, 2009, **113**, 3056-3061.
- 16 61. T. Muthulakshmi, P. Maheshwari, D. Dutta, A.K. Bera, M.N. Singh, A.K. Sinha, S.M.
17 Yusuf, P.K. Pujari, *Phys. Chem. Chem. Phys.*, 2020, **22**, 14309.
- 18 62. K. Morishige, H. Uematsu, *J. Chem. Phys.*, 2005, **122**, 044711.
- 19 63. K. Morishige, K. Kawano, *J. Chem. Phys.*, 1999, **110**, 4867-4872.
- 20 64. C. Benmore, L.C. Gallington, E. Soignard, *Mol. Phys.*, 2019, **117**, 2470-2476.
- 21 65. G. Camisasca, H. Pathak, K.T. Wikfeldt, L.G. Pettersson, *J. Chem. Phys.*, 2019, **151**,
22 044502.

- 1 66. L. B. Skinner, C.J. Benmore, J.C. Neufeind, J.B. Parise, *J. Chem. Phys.*, 2014, **141**,
2 214507.
- 3 67. H. Pathak, A. Späh, K.H. Kim, I. Tsironi, D. Mariedahl, M. Blanco, S. Huotari, V.
4 Honkimäki, A. Nilsson, *J. Chem. Phys.*, 2019, **150**, 224506.
- 5 68. J. Neufeind, C.J. Benmore, J.K.R. Weber, D. Paschek, *Mol. Phys.*, 2011, **109**, 279-288.
- 6 69. J. L. Finney, D.T. Bowron, A.K. Soper, T. Loerting, E. Mayer, A. Hallbrucker, *Phys.*
7 *Rev. Lett.*, 2002, **89**, 205503.
- 8 70. J. L. Finney, A. Hallbrucker, I. Kohl, A.K. Soper, D.T. Bowron, *Phys. Rev. Lett.*, 2002,
9 **88**, 225503.
- 10 71. P. A. Bonnaud, B. Coasne, R.J. Pellenq, *J. Phys. Condens. Mat.*, 2010, **22**, 284110.
- 11 72. K. Shirono, H. Daiguji, *J. Phys. Chem. C*, 2007, **111**, 7938-7946.
- 12 73. A. A. Milischuk, B.M. Ladanyi, *J. Chem. Phys.*, 2011, **135**, 174709.
- 13 74. K. Koga, G.T. Gao, H. Tanaka, X.C. Zeng, *Nature*, 2001, **412**, 802-805.
- 14 75. T. Le, A. Striolo, D.R. Cole, *J. Phys. Chem. C*, 2015, **119**, 15274-15284.
- 15 76. T. T. B. Le, A. Striolo, S.S. Gautam, D.R. Cole, *Langmuir*, 2017, **33**, 11310-11320.
- 16 77. G. T. Gao, X.C. Zeng, H. Tanaka, *J. Chem. Phys.*, 2000, **112**, 8534-8538.
- 17 78. K. Koga, X.C. Zeng, H. Tanaka, *Phys. Rev. Lett.*, 1997, **79**, 5262.
- 18 79. P. Kumar, S.V. Buldyrev, F.W. Starr, N. Giovambattista, H.E. Stanley, *Phys. Rev. E*,
19 2005, **72**, 051503.
- 20 80. R. Zangi, *J. Phys. Condens. Mat.*, 2004, **16**, S5371.
- 21 81. S. Han, P. Kumar, H.E. Stanley, *Phys. Rev. E*, 2008, **77**, 030201.
- 22 82. K. T. Gillen, D.C. Douglass, M.J.R. Hoch, *J. Chem. Phys.*, 1972, **57**, 5117-5119.
- 23 83. Y. Liu, Q. Wang, *Phys. Rev. B*, 2005, **72**, 085420.

- 1 84. Y. Liu, Q. Wang, T. Wu, L. Zhang, *J. Chem. Phys.*, 2005, **123**, 234701.
- 2 85. Y. C. Liu, Q. Wang, L.H. Lu, *Chem. Phys. Lett.*, 2003, **381**, 210-215.
- 3 86. A. Fouzri, R. Dorbez-sridi, M. Oumezzine, *J. Chem. Phys.*, 2002, **116**, 791-797.
- 4 87. P. Smirnov, T. Yamaguchi, S. Kittaka, S. Takahara, S. Kuroda, *J. Phys. Chem. B*, 2000,
5 **104**, 5498–5504.
- 6 88. K. Yoshida, T. Yamaguchi, S. Kittaka, M. C. Bellissent-Funel, P. Fouquet, *J. Chem.*
7 *Phys.*, 2008, **129**, 054702.
- 8 89. A. Fouzri, R. Dorbez-Sridi, M. Oumezzine, *Eur. Phys. J. Appl. Phys.*, 2003, **22**, 21-28.

9

10

11

12

13

14

15

16

17

18 **Table 1.** Comparison of ‘r’ values for first and second coordination shells of O-O bonds for
19 confined ice structures between 200-250 K, and 273 K with those reported in the literature

20

First shell (r (Å))	Second shell (r (Å))	Measurement approach	Confinement	Type of Ice	Ref.
------------------------	-------------------------	-------------------------	-------------	-------------	------

T = 200 - 250 K					
2.8	4.6	Experimental	SBA-15 (pore = 6 nm, 8 nm)	Crystalline	This work
2.78 ± 0.03	4.52 ± 0.02	MD simulations	Silica (pore = 4 nm, 6nm, 8 nm)	Crystalline	This work
2.9	4.5	Experimental	Vycor glass (pore = 4 nm)	Crystalline	Ref. 86
2.78	4.26	Experimental	MCM-41 (pore = 2.8 nm)		Ref. 87
2.36	4.6	Experimental	MCM-41 (pore = 2.83 nm)	Non-crystalline	Ref. 88
2.8	4.1	Experimental @ 77K	Silica gel (pore = 6 nm) 20% hydrated	Crystalline	Ref. 89
T = 273 K					
2.8	4.6	Experimental	SBA-15 (pore = 6 nm, 8 nm)		This work
2.78 ± 0.03	4.52 ± 0.02	MD simulations	Silica (pore = 4 nm, 6nm, 8 nm)		This work
2.9	4.5	Experimental	Vycor glass (pore = 4 nm)		Ref. 86
2.76	4.15	Experimental	MCM-41 (pore = 2.8 nm)		Ref. 87
2.36	4.6	Experimental	MCM-41 (pore = 2.83 nm) @ 268K		Ref. 88

1

2

3

4

5

6

7

8 Captions for figures

9 **Figure 1.** (a) Schematic representation of the experimental setup for Wide-Angle X-Ray
 10 Scattering (WAXS) measurements and (b) the snapshot represents the geometry of the
 11 cylindrical silica pore with a diameter of 4 nm and confined water molecules. Silica and water

1 atoms are shown by the VDW and CPK drawing methods, respectively, implemented in VMD
2 visualization software.

3 **Figure 2.** Identification of the crystalline features of ice in Wide-Angle X-ray Scattering
4 (WAXS) patterns. Crystalline ice is observed in silica (SBA-15) nanopores with pore diameters
5 of 4 nm, 6 nm, and 8 nm at temperatures ranging from 183 K to 273 K. (*) indicates dominant
6 cubic ice phase with minor hexagonal ice contribution.

7 **Figure 3.** X-ray differential pair distribution functions of O-O and O-H interactions of confined
8 water in 6 nm and 8 nm sized pores as a function of temperature.

9 **Figure 4.** The radial distribution function of oxygen-oxygen atoms in water molecules in 4 nm
10 (a), 6 nm (b) and 8 nm (c) silica pores. The corresponding coordination number of oxygen-
11 oxygen in 4 nm (d), 6 nm (e) and 8 nm (f) silica pores as a function of the temperature are
12 obtained from molecular dynamics simulations to determine the isosbestic point of water in
13 confinement.

14 **Figure 5.** Snapshots representing the front and side views of the formed hexagonal ice structures
15 in silica nanopores with diameters of 4 nm (a and b) and 8 nm (c and d) and cubic ice in 4 nm (e
16 and f) obtained from the molecular dynamics simulations. The snapshots were taken at a
17 temperature of 200 K. Structured water molecules are shown using VDW representation and
18 implemented in the VMD visualization software.

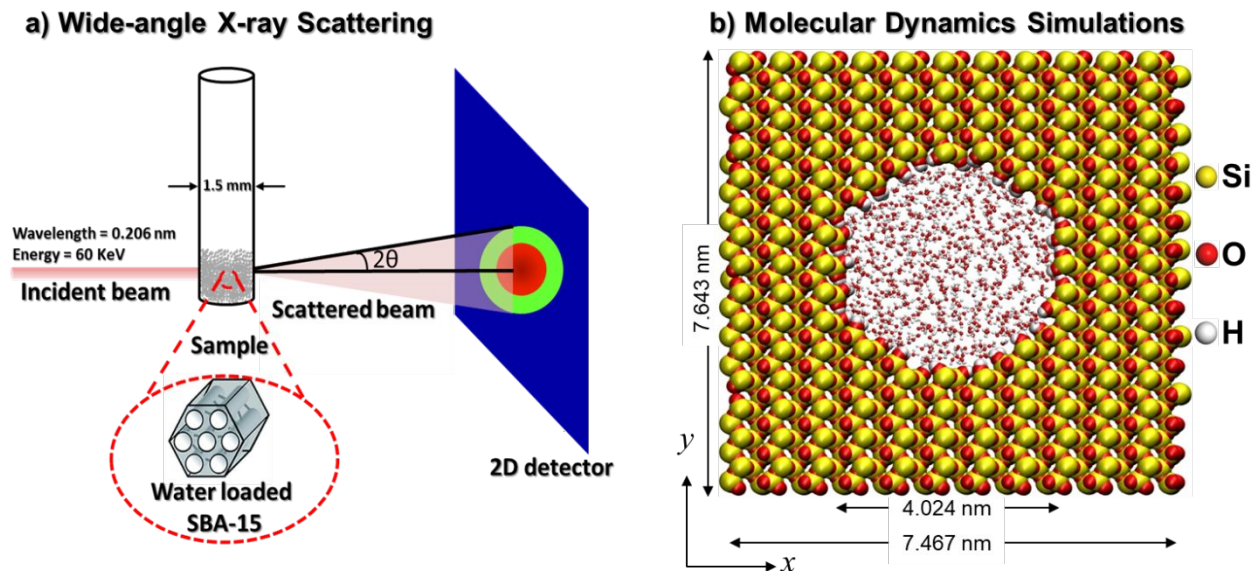
19 **Figure 6.** The density maps of the confined water molecules show the progressive melting of the
20 confined ice as the temperature increase in 4 nm, 6 nm and 8 nm silica pores. The density maps
21 are averaged over the entire 10 ns of the temperature of interest.

22 **Figure 7.** The number of water-water hydrogen bonds normalized by the number of the
23 simulated water molecules as a function of temperature and simulation time are shown in (a).
24 The total number of hydrogen bonds between the interfacial water molecules and the hydroxyl
25 groups in the pore surface as a function of temperature and the simulation time are shown in (b).

26 **Figure 8.** The residence autocorrelation function of water molecules in 4 nm (a), 6 nm (b) and 8
27 nm (c) silica pores as a function of the contact time. The residence autocorrelation function is
28 averaged over the entire 10 ns of the simulation time at each temperature.

29 **Figure 9.** Potential energy associated with the interactions of the water molecules normalized by
30 the total number of water molecules in 4 nm, 6 nm and 8 nm silica pores are shown (a). The
31 steep changes in the potential energy profiles are shaded to emphasize the regions where the
32 first-order transitions occur. The interaction energy of interfacial water molecules with the
33 surface of 4 nm, 6 nm and 8 nm silica pores are shown (b).

34 **Figure 10.** The self-diffusion coefficients of confined water along the pore length (D_z) as a
35 function of the temperature and the pore diameter predicted from molecular dynamics
36 simulations are shown. The error bars represent the standard deviations based on simulations
37 performed in triplicate.

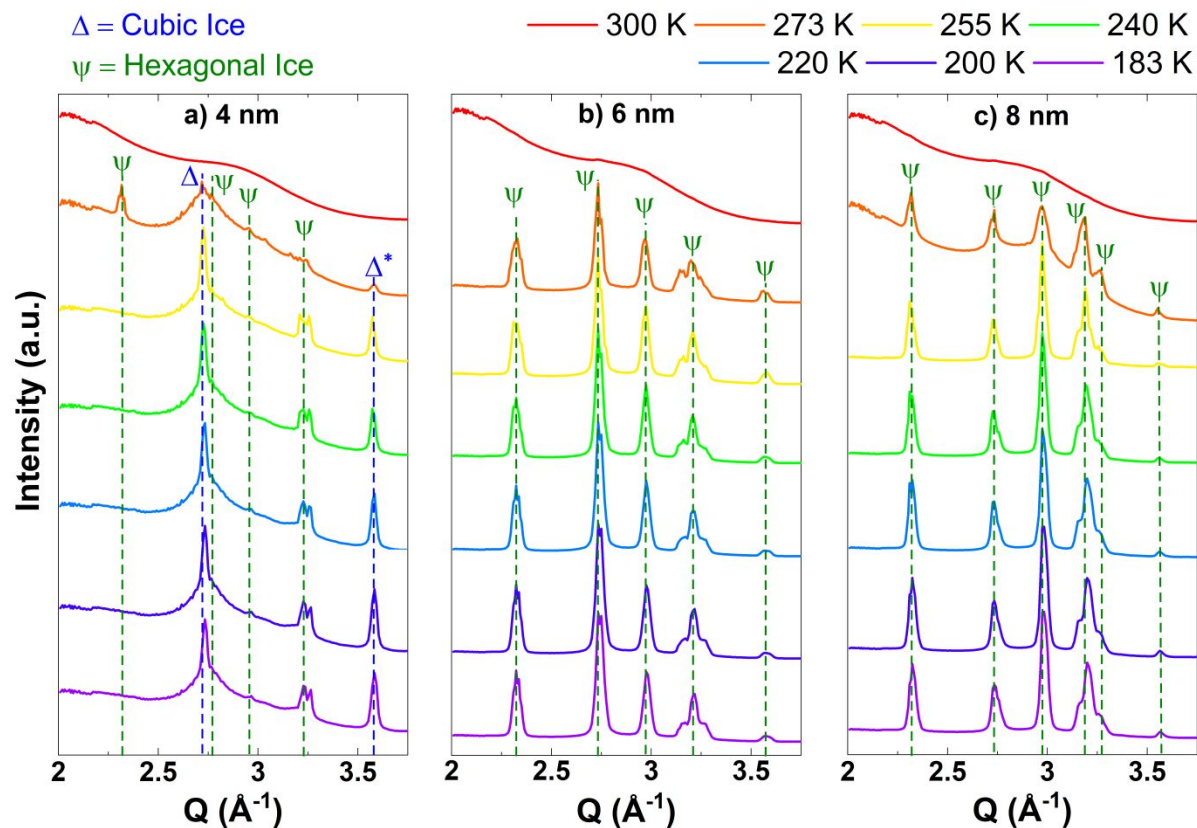


1

2

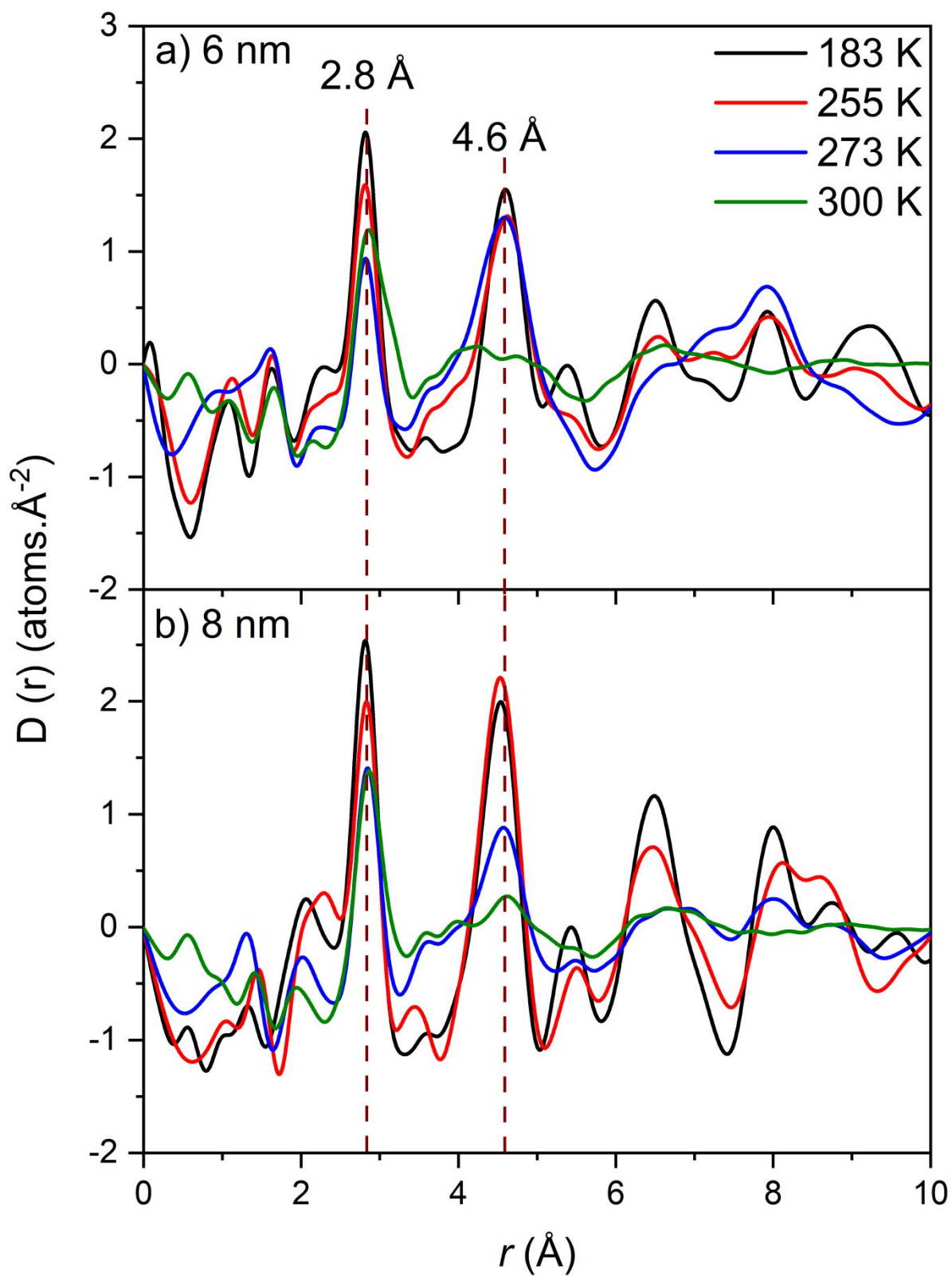
3 **Figure 1.** (a) Schematic representation of the experimental setup for Wide-Angle X-Ray
4 Scattering (WAXS) measurements and (b) the snapshot represents the geometry of the
5 cylindrical silica pore with a diameter of 4 nm and confined water molecules. Silica and water
6 atoms are shown by the VDW and CPK drawing methods, respectively, implemented in VMD
7 visualization software.

8

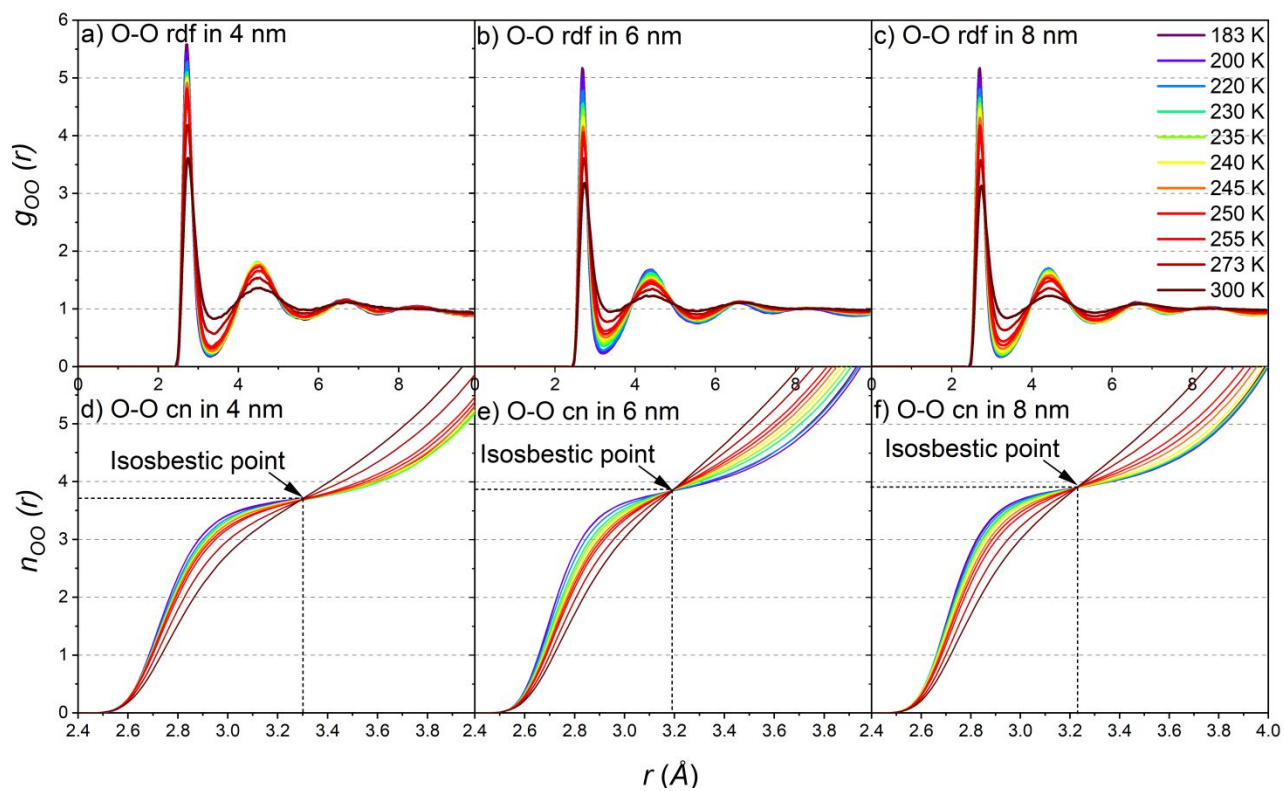


1
 2 **Figure 2.** Identification of the crystalline features of ice in Wide-Angle X-ray Scattering
 3 (WAXS) patterns. Crystalline ice is observed in silica (SBA-15) nanopores with pore diameters
 4 of 4 nm, 6 nm, and 8 nm at temperatures ranging from 183 K to 273 K. (*) indicates dominant
 5 cubic ice phase with minor hexagonal ice contribution.

6
 7
 8
 9

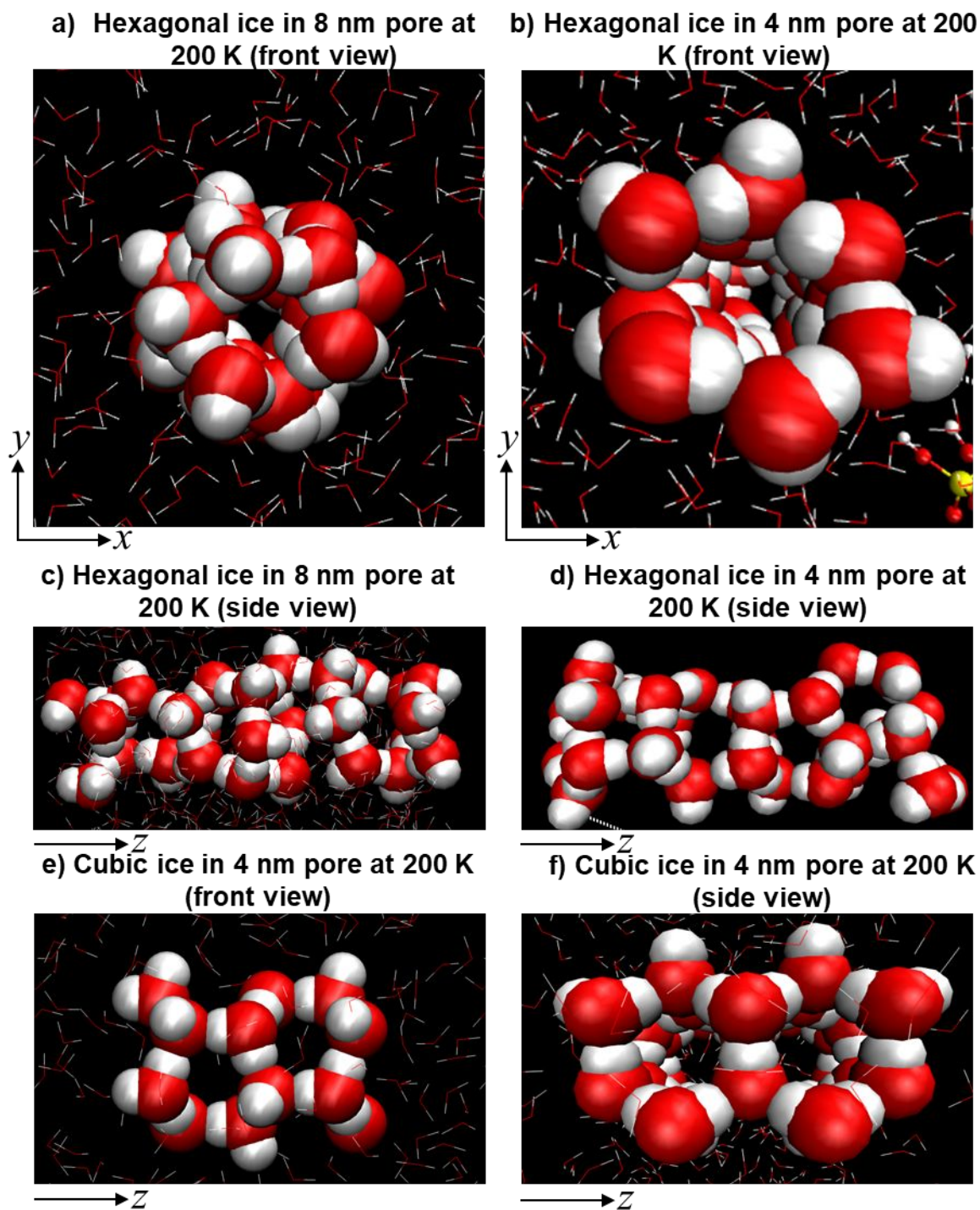


1
2 **Figure 3.** X-ray differential pair distribution functions of O-O and O-H interactions of confined
3 water in 6 nm and 8 nm sized pores as a function of temperature.

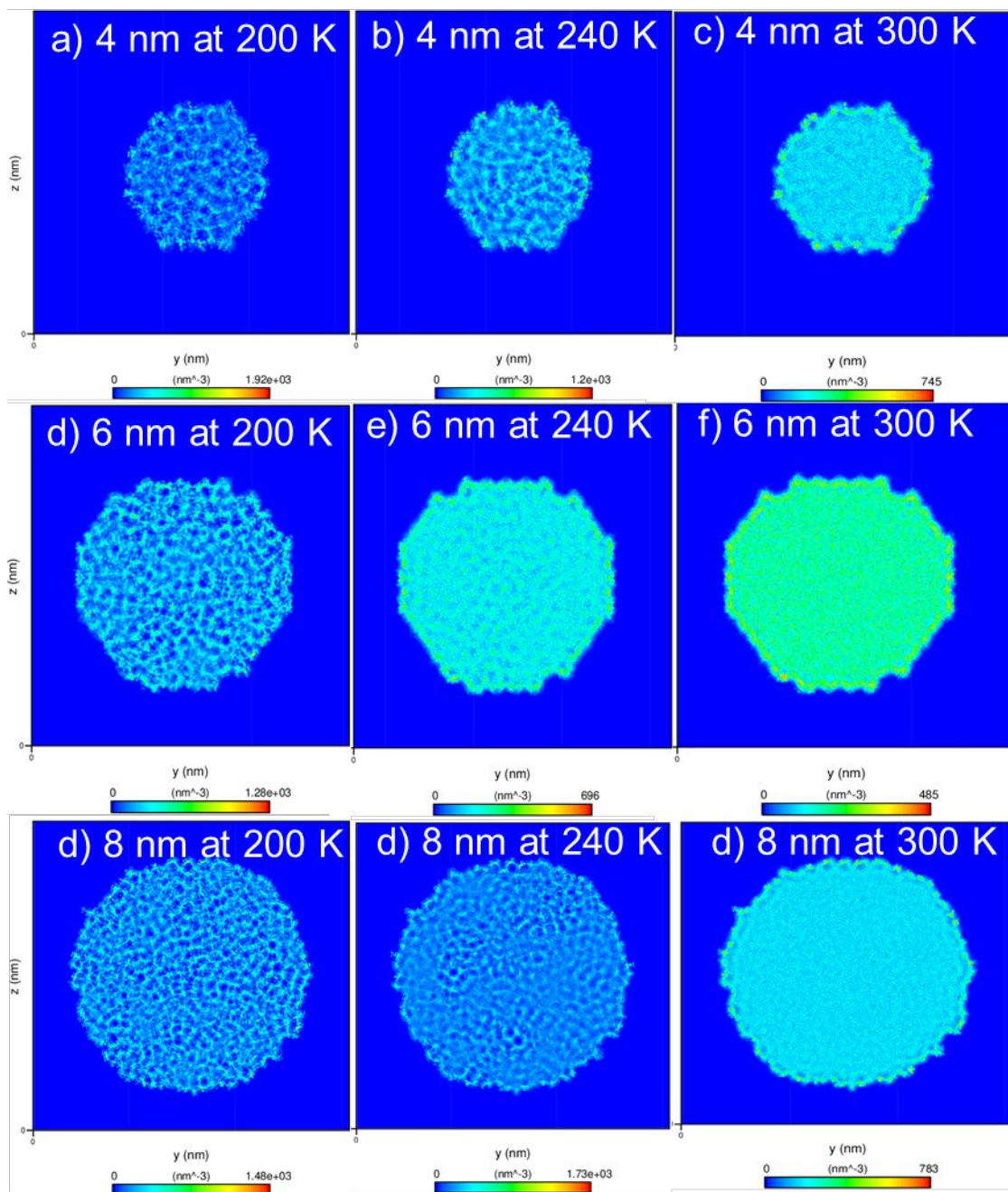


1
 2 **Figure 4.** The radial distribution function of oxygen-oxygen atoms in water molecules in 4 nm
 3 **(a)**, 6 nm **(b)** and 8 nm **(c)** silica pores. The corresponding coordination number of oxygen-
 4 oxygen in 4 nm **(d)**, 6 nm **(e)** and 8 nm **(f)** silica pores as a function of the temperature are
 5 obtained from molecular dynamics simulations to determine the isosbestic point of water in
 6 confinement.

7



1
2 **Figure 5.** Snapshots representing the front and side views of the formed hexagonal ice structures
3 in silica nanopores with diameters of 4 nm (**a and b**) and 8 nm (**c and d**) and cubic ice in 4 nm (**e**
4 **and f**) obtained from the molecular dynamics simulations. The snapshots were taken at a
5 temperature of 200 K. Structured water molecules are shown using VDW representation and
6 implemented in the VMD visualization software.

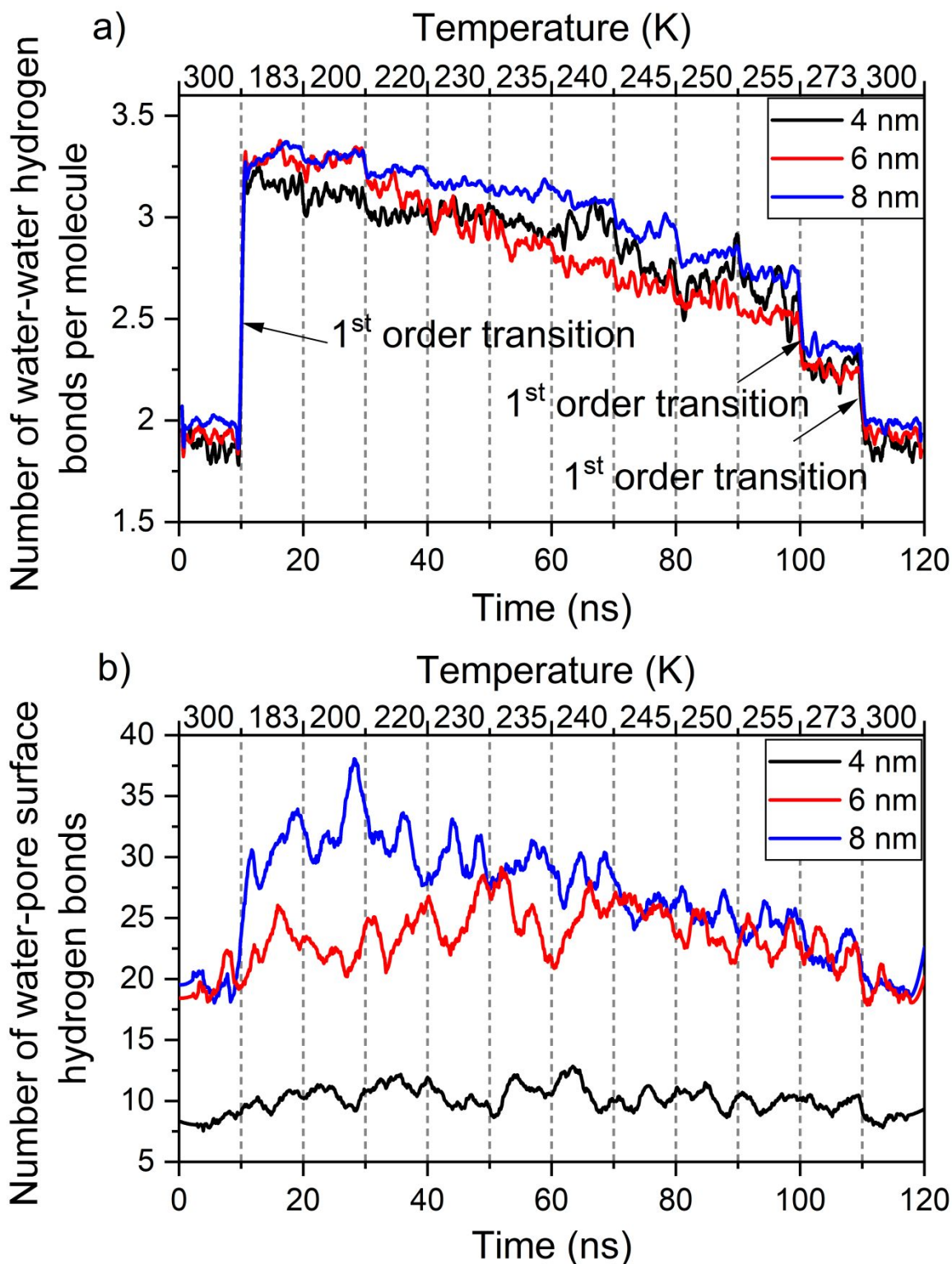


1

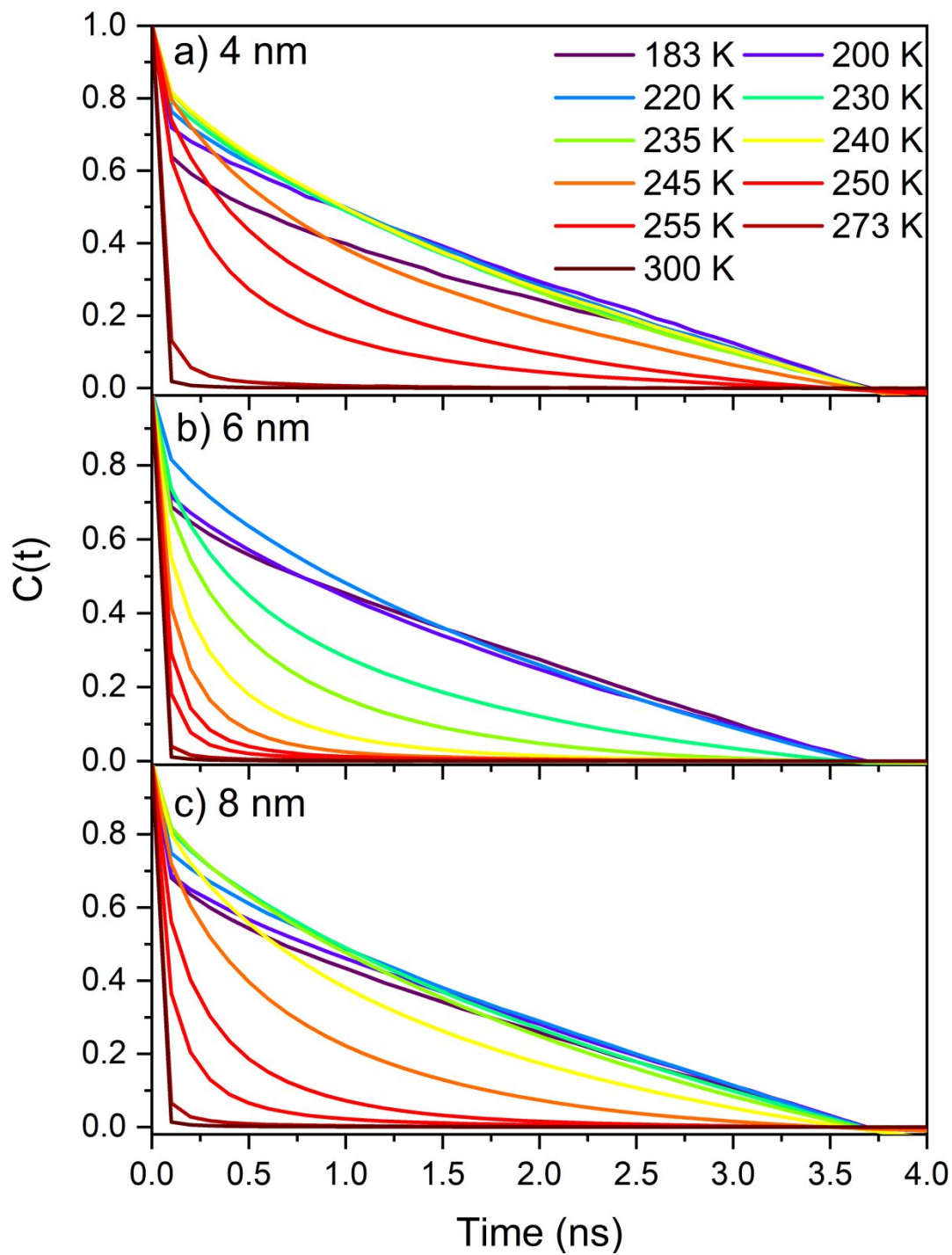
2

3 **Figure 6.** The density maps of the confined water molecules show the progressive melting of the
 4 confined ice as the temperature increase in 4 nm, 6 nm and 8 nm silica pores. The density maps
 5 are averaged over the entire 10 ns of the temperature of interest.

6



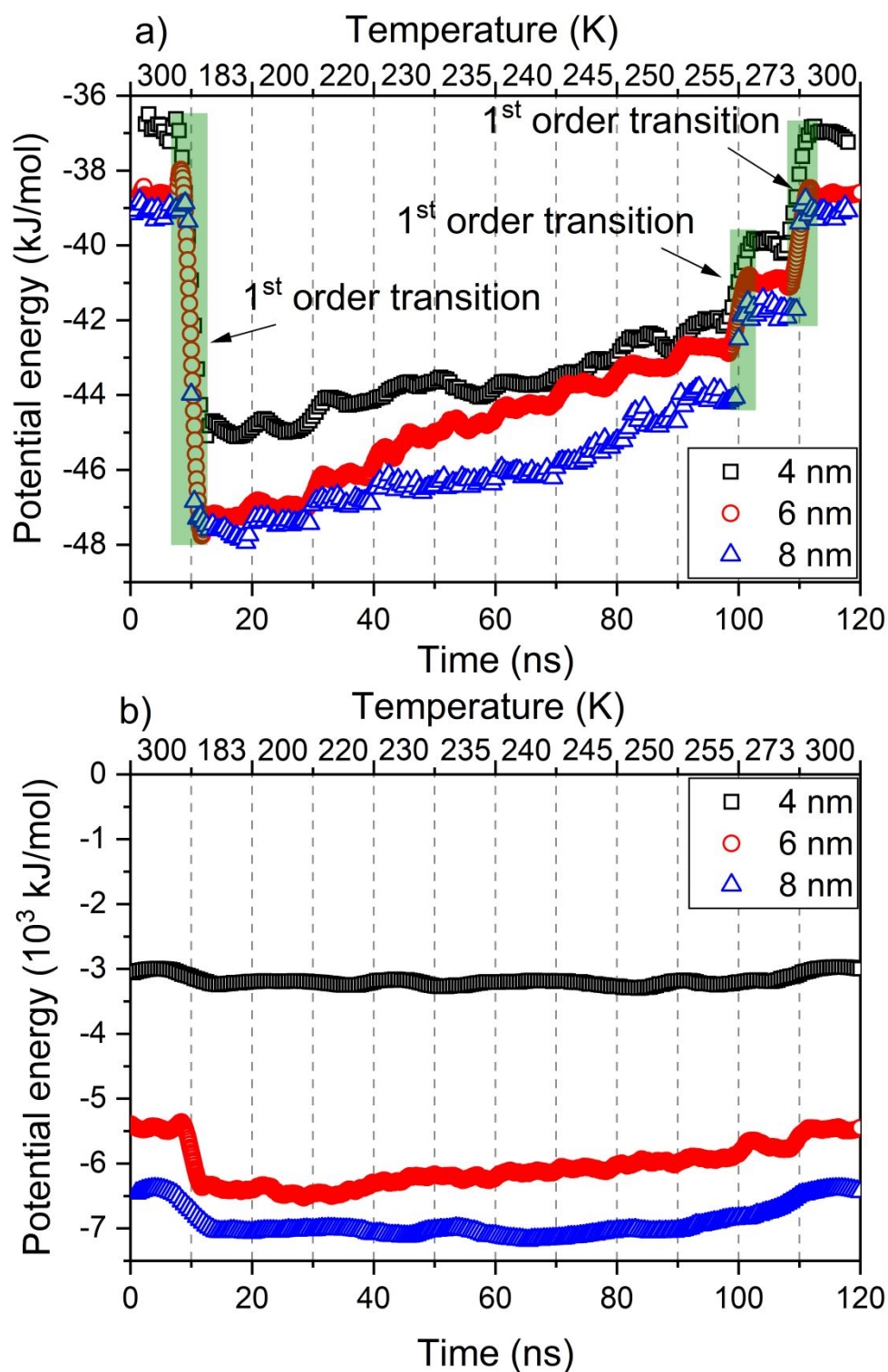
1
 2 **Figure 7.** The number of water-water hydrogen bonds normalized by the number of the
 3 simulated water molecules as a function of temperature and simulation time are shown in **(a)**.
 4 The total number of hydrogen bonds between the interfacial water molecules and the hydroxyl
 5 groups in the pore surface as a function of temperature and the simulation time are shown in **(b)**.



1

2 **Figure 8.** The residence autocorrelation function of water molecules in 4 nm (a), 6 nm (b) and 8
3 nm (c) silica pores as a function of the contact time. The residence autocorrelation function is
4 averaged over the entire 10 ns of the simulation time at each temperature.

5



1
 2 **Figure 9.** Potential energy associated with the interactions of the water molecules normalized by
 3 the total number of water molecules in 4 nm, 6 nm and 8 nm silica pores are shown (a). The
 4 steep changes in the potential energy profiles are shaded to emphasize the regions where the
 5 first-order transitions occur. The interaction energy of interfacial water molecules with the
 6 surface of 4 nm, 6 nm and 8 nm silica pores are shown (b).

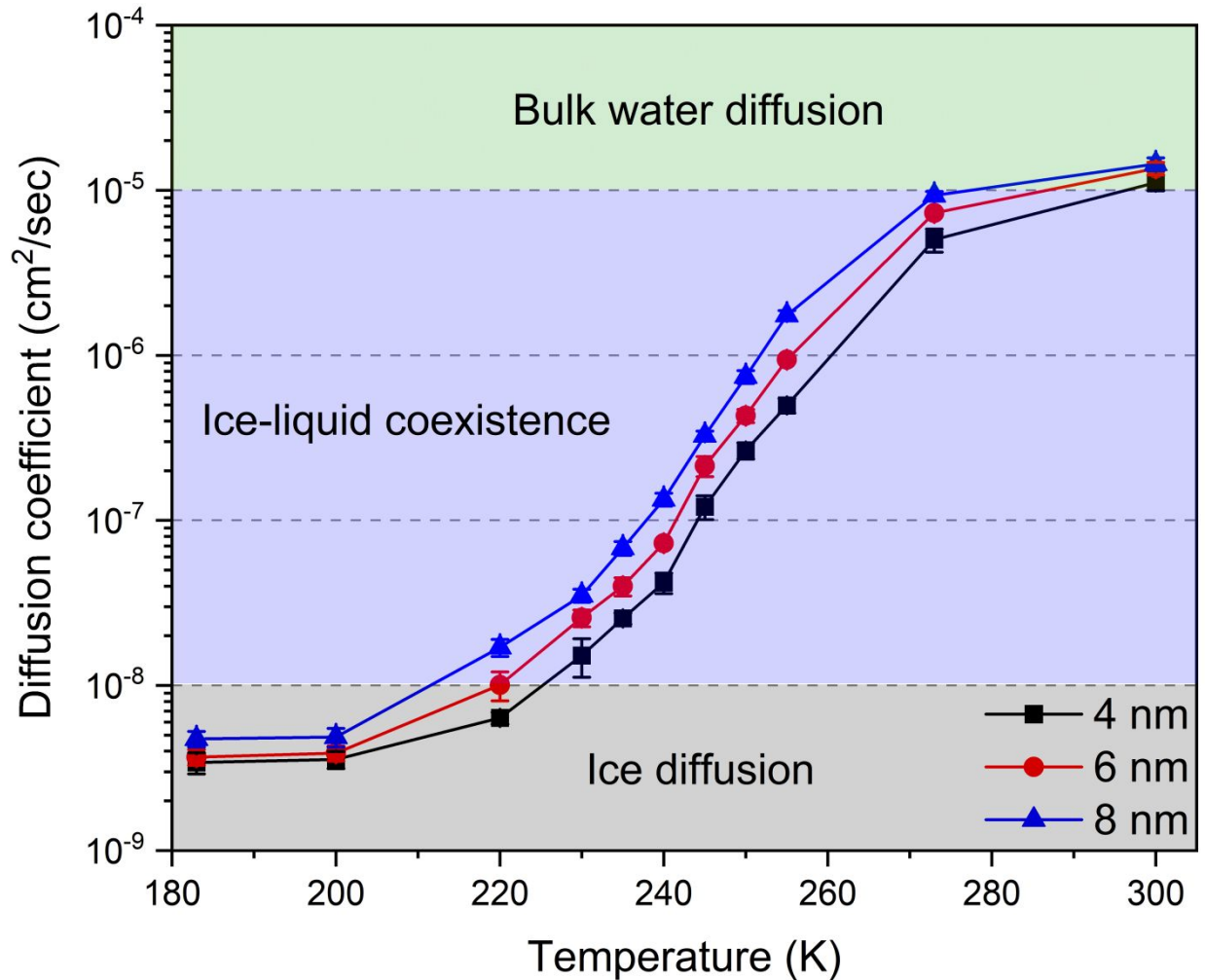
1
2
34
5
6
7
8
9
10
11
12
13
14

Figure 10. The self-diffusion coefficients of confined water along the pore length (D_z) as a function of the temperature and the pore diameter predicted from molecular dynamics simulations are shown. The error bars represent the standard deviations based on simulations performed in triplicate.